Structural characterization of $La_{1-x}MnO_{3\pm\delta}$ by x-ray diffraction and x-ray absorption spectroscopy

G. Dezanneau, M. Audier, and H. Vincent
Laboratoire des Matériaux et du Génie Physique, BP46, Domaine Universitaire, F-38402 Saint Martin d'Hères Cedex, France

C. Meneghini*
Dipartimento di Fisica, Università di "Roma Tre," Via della Vasca Navale, 84 I-00146 Roma, Italy and INFM-OGG c/o ESRF, Grenoble, France

E. Djurado
Laboratoire d'Electrochimie et de Physico-chimie des Matériaux et Interfaces, 1130, rue de la Piscine, Domaine Universitaire, F-38402, Saint Martin d'Hères Cedex, France

(Received 30 January 2003; revised manuscript received 17 September 2003; published 23 January 2004)

Structural and magnetic properties of nanocrystalline compounds of the general formula $La_{1-x}MnO_{3+\delta}$ have been investigated combining x-ray diffraction and x-ray absorption spectroscopy in order to achieve an accurate description of the sample atomic structure in relation with its magnetic properties. The study reveals the segregation of different phases instead of a homogeneous sample composition. Interesting is the segregation of a vacancy-doped phase La_yMnO_3 whose composition is the same ($y\sim0.9$) for all the investigated samples, independently of the average sample composition. Since this phase is found to be principally responsible for the magnetic properties of these compounds, such a phase separation explains the largely composition-independent magnetic properties observed in the range $0.9\geqslant La/Mn\geqslant0.7$.

DOI: 10.1103/PhysRevB.69.014412 PACS number(s): 75.47.Lx, 61.10.Nz, 61.10.Ht

I. INTRODUCTION

Rare-earth based mixed-valence manganites stimulated a large interest owing to their peculiar magnetotransport properties and, in particular, to the colossal magnetoresistance (CMR) effect.[1] In recent years large efforts have been devoted to understand the physics involved in the magnetic and transport properties of these materials.[2] These compounds are solid solutions of general formula, $RE_{1-x}ME_xMnO_3$, in which partial substitution of rare-earth (RE) ions (like La, Pr, Nd, or Y) with divalent metals (ME), such as Ca, Sr, Ba, produces mixed-valence Mn^{3+}-Mn^{4+} phases. The parent compounds $REMnO_3$ and $MEMnO_3$ are insulating materials that antiferromagnetically order at low temperatures ($T<T_N$). The mixed valence activates the double-exchange (DE) interaction which promotes ferromagnetic coupling between Mn^{3+} and Mn^{4+} ions[3–5] giving rise to the magnetoresistance effect. Some of these compounds (in the composition range $0.2\leqslant x<0.5$) undergo an insulator to metal transition as a function of temperature (T_{MI}), close to the Curie temperature (T_C). The closeness of T_C and T_{MI} produces the so-called colossal magnetoresistance effect. The Mn^{3+}-Mn^{4+} mixed-valence state can also be obtained by changing the stoichiometry, as for the so-called *self-doped* or *vacancy-doped* compounds of general formula $La_{1-x}Mn_{1-y}O_{3+\delta}$. In these compounds changes in x, y, and δ modify the Mn^{3+}/Mn^{4+} ratio activating the DE interaction; this promotes the ferromagnetic (FM) coupling and can give rise to CMR effect as in substituted compounds.[6,7] In the field of self-doped manganites, nanocrystalline compounds are of strong interest due to their enhanced magnetoresistance properties in low fields and to their high potential as electrode material in solid oxide fuel cells (SOFC) or in yttria stabilized zirconia (YSZ) based gas sensors.[8,9]

The substituted compounds have been extensively investigated and their structural, magnetic, and transport properties as a function of temperature and composition are widely characterized in the literature. On the contrary, the vacancy-doped compounds are less accurately described, and discrepancies are reported in the literature.[10–16] At the origin of these widespread results is the complexity of these materials from a cristallochemistry point of view. This makes it difficult to understand how the structure evolves to accommodate vacancies and nonstoichiometry. The lanthanum manganite compounds may exhibit oxidative nonstoichiometry usually reflected by the formula $LaMnO_{3+\delta}$. In the case of positive δ this formula is ambiguous since cation vacancies must be considered instead of interstitial oxygen anions; the formula should then be written as $(LaMn)_{1-x}O_3$ [with $x=\delta/(3+\delta)$]. The so-called oxygen excess δ depends on synthesis and thermal treatment conditions: the highest δ values are obtained at low temperature and in highly oxidative atmosphere. Values of δ as high as 0.15 are frequently reported, which is also equivalent to about 5% of La and Mn vacancies. Much higher δ (i.e., $\delta\approx0.26$–0.27) values have also been proposed,[10,11] equivalent to about 9% of La and Mn vacancies. Studies on $La_{1-x}MnO_{3\pm\delta}$ compounds (with $0\leqslant x\leqslant0.3$) have shown structural and magnetic properties widely dispersed even for compounds of very similar compositions.[12–16] For example, studies reporting a single $La_{1-x}MnO_{3\pm\delta}$ phase with $x\approx0.2$ (Refs. 12 and 13) contrast with the pseudobinary phase diagram for La_2O_3-Mn_2O_3 solutions[17] that assigns a lower limit of 0.9 to the La/Mn ratio implying, for $x>0.1$, a phase separation between a per-

TABLE I. Results on sample composition, microstructural, and magnetic properties.

	La/Mn [a]	La/Mn [b]	Mn^{4+} at. % [c]	Overall composition	Particle size (μm) [d]	Crystallite size (nm) [e]	T_C (K)
S_1	1.0	0.98(1)	39(2)	$La_{0.93}Mn_{0.95}O_3$	0.48(2)	43(6)	212(2)
$S_{0.9}$	0.9	0.89(1)	31(2)	$La_{0.89}MnO_{2.99}$	0.51(2)	40(6)	248(2)
$S_{0.8}$	0.8	0.80(1)	31(2)	$La_{0.80}MnO_{2.85}$	0.47(2)	33(5)	252(2)
$S_{0.7}$	0.7	0.67(1)	22(2)	$La_{0.67}MnO_{2.615}$	0.48(2)	27(5)	249(2)

[a]Atomic ratio in the precursor solution.
[b]Atomic ratio determined by induced coupled plasma (ICP).
[c]Mn^{4+} concentration determined from titration (in at. % of the total of Mn atoms).
[d]Determined form laser granulometry.
[e]Determined from XRD applying the Scherrer law on (024) reflection (hexagonal setting).

ovskite phase $La_{\sim 0.9}MnO_3$, and a manganese oxide phase such as, for example, Mn_3O_4.[18] The complexity of self-doped manganese perovskites requires a special care in order to understand the close relations among composition, structure, and magnetic properties. In addition, dealing with nanocrystalline materials, surface/interface effects as well as the presence of parasitic phases, which may evade detection due to the small crystallite size, must be taken into account for a deep comprehension of the sample properties.

Ultrasonic assisted spray pyrolysis (UASP) (Refs. 19 and 20) has been used to produce self-doped manganese oxide perovskites with the advantage of providing a large amount of material with a precise reproducibility of microstructural properties, particle morphology (grain size and shape), and crystallographic structure.[21,22] A peculiar aspect of these compounds is that the Curie temperature and the sharpness of the ferromagnetic (FM) transition increase as the average La/Mn ratio decreases down to La/Mn$\sim$0.9. Below this value T_C remains almost unchanged. In addition, the saturation magnetization reaches a maximum value for La/Mn $\sim$0.9. The aim of this work is to shed light on these peculiar trends through an accurate description of the atomic structure of vacancy-doped $La_{1-x}MnO_{3+\delta}$ nanocrystalline compounds. To this end we employed composition measurements, transmission electron microscopy (TEM), x-ray diffraction (XRD), and x-ray absorption spectroscopy (XAS) techniques. Emphasis has been given to the complementary information derived from Rietveld refinements of XRD patterns and accurate analysis of XAS spectra.

II. MATERIALS AND METHODS

A. Sample preparation, chemical, and magnetic characterization

Four $La_{1-x}MnO_{3+\delta}$ samples ($x=0$, 0.1, 0.2, 0.3, and $-0.385 \leqslant \delta \leqslant 0$) were produced by UASP. This technique, which has been widely used for the production of fine electroceramic materials such as ZrO_2, TiO_2, and PZT,[19–21] involves the high-temperature pyrolysis of an aerosol in a tubular furnace. The precursor solution consisted of lanthanum and manganese nitrates hexahydrates $[La(NO_3)_3 \cdot 6H_2O$ and $Mn(NO_3)_3 \cdot 6H_2O]$ dissolved in distilled water at 0.025 mol/l concentration. The aqueous solution was atomized by piezoelectric ceramic transducers, working at 1.7-MHz frequency. A pure air flow (6 l/min) carried the aerosol through a tubular furnace heated at 900 °C. The final powders were then collected in an electrostatic receptor at the furnace exit. The ratios between La and Mn in the precursor solutions (Table I) were fixed to those of the target compounds. In the following we will refer to each sample using the La/Mn ratio in its precursor solution: S_1, $S_{0.9}$, $S_{0.8}$, and $S_{0.7}$.

The effective La/Mn ratio in the final compound was measured by induced coupled-plasma (ICP) atomic spectroscopy and resulted to be close to that of the precursor solution (see Table I). The Mn^{4+} content, measured by iodometry,[23] decreases from 39% in S_1, to 22% in $S_{0.7}$. It is intriguing that the lower values of Mn^{4+} content are found for the larger vacancy doping of the lanthanum site. Such an apparently anomalous result had been already noted in Refs. 12–14 where it was suggested that the charge deficit due to vacancies on La sites would be preferably compensated by the formation of oxygen vacancies, rather than by oxidation of Mn^{3+} into Mn^{4+}. Another possible explanation is that decreasing the La content brings the La/Mn ratio in a region of the phase diagram where a phase separation occurs.[17] Thus for La/Mn <0.9, the decreasing of Mn^{4+} concentration measured by iodometry might be related to the occurrence of parasitic manganese oxide phases with different Mn stoichiometry such as Mn_3O_4 and/or Mn_2O_3 in which the average valence of Mn is only 2.66 and 3, respectively.

Powder particle morphology has been probed by scanning electron microscopy (SEM) and transmission electron microscopy (TEM) showing that the powders consist of submicrometer particles having perfect spherical shape (Fig. 1). The particle size distribution has been measured by optical granulometry leading to similar average diameters of $\sim$0.5 μm for all compositions as reported in Table I. The particle size distribution produced by UASP mainly depends on synthesis parameters such as temperature and the ultrasonic frequency. The very similar particle size distributions observed in our samples originates from the very same synthesis procedure adopted for all the compositions.

The bright field TEM image presented in Fig. 1 also evidences a crystalline contrast, indicating that spherical particles are composed of many nanometric crystallites. The av-

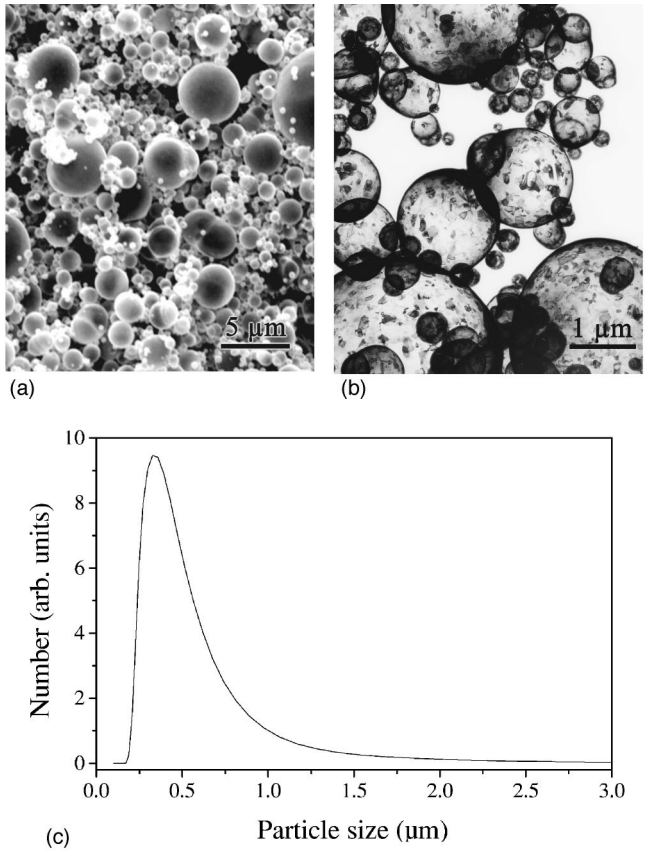

FIG. 1. Morphology of sample $S_{0.9}$ as it appears from SEM (upper left panel) and TEM (upper right panel), and distribution of particle size from laser granulometry (lower panel).

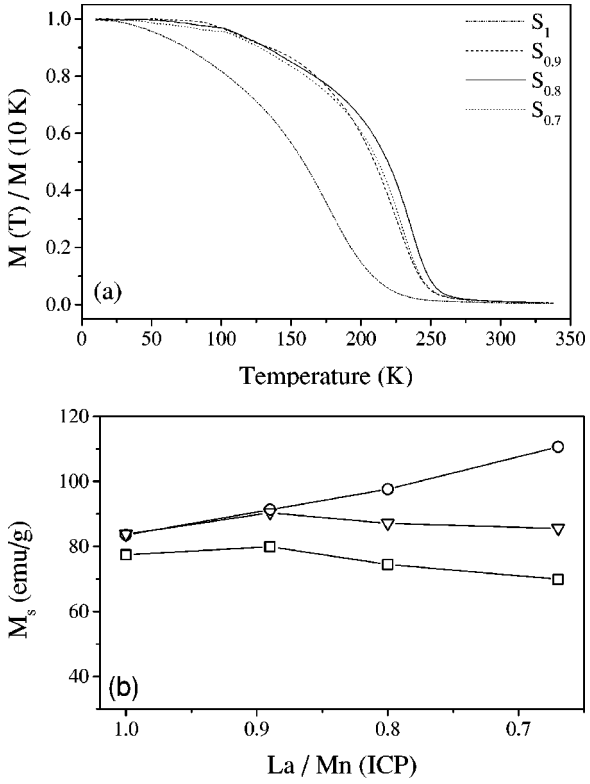

FIG. 2. (a) Magnetization as a function of temperature, under excitation field of 0.2 T; (b) M_S measured at 10 K and under 8 T (open squares), calculated from overall sample composition (open circles) and calculated from phase-separation models deduced from Rietveld analysis (open triangles).

erage crystallite (coherently diffracting regions) size was determined by applying the Scherrer law on the (024) XRD peak ($R\bar{3}c$ hexagonal setting, see below), and results in a few tens of nm. The crystallite size decreases when the La/Mn ratio is reduced, a trend likely to be related to the above-mentioned solubility limit for La vacancies of about 10% (Ref. 17) (i.e., La/Mn $\sim$0.9). In this case the larger La deficit in the precursor solution would contrast the growth of the perovskite phase.

Magnetic characterizations were performed on a vibrating sample magnetometer in the temperature range 10–340 K and magnetic field between 0 and 8 T. All the vacancy doped samples, S_1–$S_{0.7}$, present a low-temperature ferromagnetic phase and become paramagnetic at high temperature [Fig. 2(a)]. The S_1 sample has the broadest magnetic transition with the lowest $T_C = 213$ K. The other samples present sharper magnetic transitions at higher $T_C \approx 250$ K which is similar to the T_C observed in standard substituted manganites near the optimum doping such as $La_{2/3}Ca_{1/3}MnO_3$.[2] In hole doped manganites T_C heavily depends on composition (notice for example that, in $La_{1-x}Ca_xMnO_3$, T_C increases from $\sim$200 K to $\sim$265 K raising x from 0.2 to 0.33) and local atomic structure around the Mn ions,[24] the similar transition T_C in $S_{0.9}$, $S_{0.8}$, and $S_{0.7}$ samples suggests they must present doped phases of similar composition/structure, despite the differences in average composition. The saturation magnetization M_s was measured at 10 K with an 8-T magnetic field [Fig. 2(b)]. M_S reaches the maximum value in the $S_{0.9}$ sample ($\sim$80 emu/g) and then decreases as the La content decreases. This finding contrasts with the values of M_s calculated assuming homogeneous samples having average composition given in Table I (column 5) which would imply a monotonic increasing trend [Fig. 2(b)] from S_1 to $S_{0.7}$. As before, this finding suggests that the overall composition is not an exhaustive parameter to characterize the sample properties. Figure 2(b) also reports the saturated magnetization as calculated from the models derived from the analysis of XRD data as described below. In this case a contribution of 42 emu/g has been considered for the Mn_3O_4 phase, when present. A much better agreement between calculated and measured M_s is found. The remaining difference is likely to be related to the small crystallite size within the samples, leading to a large influence of nonmagnetic grain-boundary regions.[25,26]

B. Crystallographic structure: x-ray diffraction

X-ray powder-diffraction patterns were collected at room temperature in the $20° < 2\theta < 120°$ range using a standard Cu-anode powder diffractometer (Siemens D500) in Bragg-Brentano geometry. A graphite monochromator and a Ni filter were used to select Cu K_α fluorescence out of the broad bremsstrahlung. The analysis of the powder XRD patterns

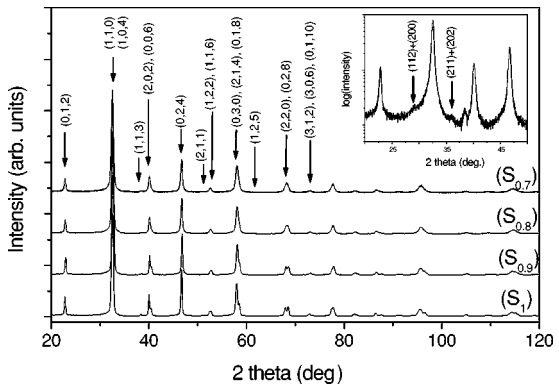

FIG. 3. Diffraction patterns for sample S_1, $S_{0.9}$, $S_{0.8}$, and $S_{0.7}$; indexation of the manganite phase is performed in $R\bar{3}c$ space group (hexagonal setting); inset: indexation of the Mn_3O_4 phase for sample $S_{0.7}$ (intensity is given in logarithmic scale).

was performed using the Rietveld[27] structural refinement approach as implemented in the FULLPROF package.[28] The background was modeled with a third-order polynomial function, while the profile of the diffraction line was modeled using a pseudo-Voigt function.

Undoped $LaMnO_3$ presents an orthorhombic structure, usually refined within the *Pnma* space group characterized by two independent oxygen positions leading to three Mn-O distances ($\sim$1.90,$\sim$1.96,$\sim$2.17 Å) and two tilting modes of the MnO_6 octahedra.[29,30] The $LaMnO_3$ structure features large distortions due to the Jahn-Teller (JT) effect on Mn^{3+} ions. Hole or vacancy doping provokes a sudden drop of the structural distortions due to the reduction of the coherent JT effect. XRD patterns of our samples (Fig. 3) were refined within the $R\bar{3}c$ (hexagonal setting) space group (no. 167) characterized by a single Mn-O distance. Within this symmetry the atomic site positions are: La (0, 0, 0.25) in $6a$; Mn (0,0,0) in $6b$, and O (x, 0, 0.25) in $18e$ with $x \simeq 0.45$. Isotropic Debye-Waller factors were independently refined on each atomic site in a last refinement run. Rietveld refinements were performed considering different models for atomic occupancies on La, Mn, and O sites. A preliminary structural refinement attempt considered the occupancies taken from the average composition measurements (as given in the ''overall composition'' column of Table I) but it did not reach a satisfactory fitting to the experimental pattern. In order to improve the refinement it was necessary to assume that the La/Mn ratio in the manganite phase could be different from the one expected from ICP measurements. The following models of cation occupancies were considered:

- Model 1 (samples $S_{0.9}$, $S_{0.8}$, $S_{0.7}$): Mn and O sites were considered fully occupied and only the La site occupancy was refined.
- Model 2 (sample S_1): starting from the best fit obtained using the model-1 La and Mn occupancies were refined in order to match the chemical analysis results.

Both these models imply the presence of parasitic phases since the refined La/Mn may differ from the overall La/Mn ratio: a Mn-rich phase is required in model 1 (samples $S_{0.9}$, $S_{0.8}$, $S_{0.7}$), a La-rich phase in model 2 (sample S_1). Table II reports results of Rietveld refinements including structural parameters and agreement factors. We observe that the oxygen thermal factors ($B_O \sim 2.5$ Å^2) are sensibly higher than those of La ($B_{La} \sim 0.8$ Å^2) and Mn ($B_{Mn} \sim 0.55$ Å^2). This should be partially related to the lower sensitivity of x rays to light atoms. However, the very large values we found here likely derive from the higher static disorder on the oxygen sites due, for example, to an incoherent Jahn-Teller effect on Mn^{3+} sites. Interestingly, the structural refinement on samples $S_{0.9}$, $S_{0.8}$, and $S_{0.7}$ (model 1) show that the La occupancy is about 0.9 for any sample considered despite the values expected from compositional analysis (ICP). This finding is in agreement with the solubility limit of La vacancies in the La_2O_3-Mn_2O_3 phase diagram, which is around 10%.[17] The segregation of Mn-rich phases, such as Mn_2O_3 and/or Mn_3O_4, must be considered in order to match the ratio La/Mn$\sim$0.9, found by Rietveld analysis, with the average sample composition as derived from ICP. These phases must be poorly crystallized or in the form of small particles since they cannot be detected in the XRD patterns except for the $S_{0.7}$ sample in which shoulders nearby the perovskite 110/101 main reflection could be associated to the Mn_3O_4 phase (see inset in Fig. 3).

We show in the following that a careful analysis of x-ray absorption spectroscopy data at the Mn *K*-edge definitively assesses the presence of a Mn_3O_4 phase. The ratio La/Mn $\sim$0.9 obtained by refining the XRD pattern of sample S_1 is considerably smaller than the value La/Mn=0.98 measured

TABLE II. Rietveld results using model 1 for samples $S_{0.9}$, $S_{0.8}$, $S_{0.7}$, and model 1 and 2 for sample S_1—fixed parameters are indicated with (*). In sample S_1, model 2 (see text), the estimated uncertainty on the Occ_{Mn} is about 1%.

Sample	S_1		$S_{0.9}$	$S_{0.8}$	$S_{0.7}$
Model	1	2	1	1	1
a (Å)	5.5146(2)	5.5146(2)	5.5127(2)	5.5075(2)	5.5070(2)
c (Å)	13.361(1)	13.361(1)	13.373(1)	13.389(1)	13.401(1)
V (Å^3)	351.88	351.88	351.67	351.73	351.96
Occ_{La}	0.920(5)	0.896*	0.908(4)	0.892(4)	0.888(3)
B_{La} (Å^2)	0.87(3)	0.88(3)	0.83(3)	0.82(3)	0.80(3)
Occ_{Mn}	1*	0.978*	1*	1*	1*
B_{Mn} (Å^2)	0.62(6)	0.65(5)	0.57(6)	0.51(5)	0.55(4)
Occ_O	1*	1*	1*	1*	1*
B_O (Å^2)	2.3(2)	2.6(2)	2.2(2)	2.8(2)	2.7(1)
x_O	0.455(1)	0.455(1)	0.454(1)	0.463(2)	0.459(1)
R_{wp}	15.4	15.4	14.6	12.6	13.6
R_{Bragg}	4.18	4.28	3.89	3.06	2.99
χ^2	3.29	3.29	2.85	2.02	2.21
R_{MnO} (Å)	1.960	1.961	1.961	1.957	1.959
θ (°)	164.5	164.2	164.4	165.7	164.7

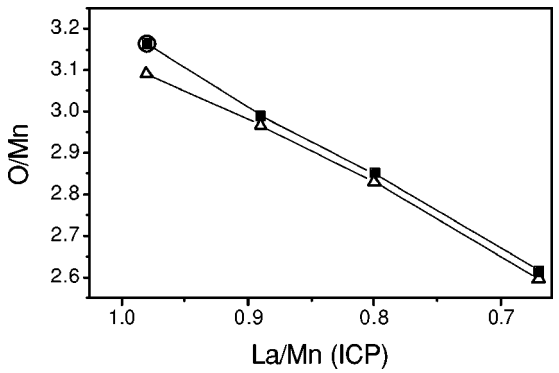

FIG. 4. Evolution of the O/Mn ratio measured by iodometry (full squares) and calculated from a phase-separation model deduced from Rietveld refinements with model 1 (open triangles) and model 2 (open circles).

by ICP. This finding implies the presence of a La-rich parasitic phase in order to preserve the overall sample composition. Such a phase has not been detected by XRD, nor by TEM, probably because, as suggested by several authors,[31,32] La-rich phases would be poorly crystalline and in the form of partially hydrolyzed oxides.

In order to verify the reliability of model 1, we calculated the average valence of the whole sample considering a mixture of a perovskite phase, of composition given by the Rietveld model, and a parasitic phase, namely La_2O_3 (for sample S_1) or Mn_3O_4 (for samples $S_{0.9}$, $S_{0.8}$, $S_{0.7}$), whose relative proportions are deduced from ICP data. In such a way we obtain a good agreement (Fig. 4) between calculated (model 1) and measured Mn^{4+} contents for samples $S_{0.9}$, $S_{0.8}$, $S_{0.7}$. In sample S_1 the larger amount of Mn^{4+} measured requires considering vacancies on both manganese and lanthanum sites (model 2). Owing to a large correlation between Mn and La occupancies the most probable La/Mn ratio, accordingly with compositional (ICP) data, was determined by looking at the iso-χ^2 maps in the space of La- and Mn-site occupancies. Further details about the procedure adopted (model 2) are given elsewhere.[22,26] As a result, for sample S_1, such an analysis suggests around 10% of vacancies on the lanthanum site and about 2% on the manganese site (Table II). We notice that, refining the pattern of sample S_1, the best fit accuracy (χ^2) decreases slightly using model 2 instead of model 1, however, we feel that model 2 is more reliable from a physical point of view since the overall sample composition deduced from it falls in agreement with ICP composition measurements.

We remark that the Mn-O distances ($R_{MnO}\sim 1.96$ Å) and Mn-O-Mn angles ($\theta\sim 164.5°$) in the refined structures vary less than 0.001 Å (0.3°) in all the samples except for sample $S_{0.8}$ having the smaller Mn-O distance (1.957 Å) and larger Mn-O-Mn angle (165.7°). This sample also presents the higher Curie temperature.

C. X-ray absorption spectroscopy

Mn *K*-edge XAS measurements were performed in transmission geometry at the CRG-GILDA beam line[33] at European Synchrotron Radiation Facility (ESRF, Grenoble, France). Measurements were carried out between 77 and 300 K in the energy range 6.2–~7 keV, corresponding to a maximum value of the photoelectron wave vector $k \sim 14$ Å^{-1} (see below). A couple of grazing incidence mirrors (energy cutoff ~10 keV) provide a harmonic free beam on the sample. X-ray beam energy was calibrated collecting XAS spectra of a pure Mn metal powder sample ($E_0 = 6537$ eV) and was regularly checked during the experiment. Incident I_o and transmitted I_1 beam intensities were collected using N_2 filled ionization chambers. Samples were prepared suspending the sample powders in ethyl alcohol (ultrasonic bath) then filtering the suspension through a millipore (Sigma-Aldrich) membrane. This procedure ensures a very homogeneous sample film, suitable for good quality XAS measurements. All four samples were measured at room temperature. The S_1, $S_{0.9}$, and $S_{0.7}$ samples were also measured at different temperatures between room temperature (RT) and liquid nitrogen (LN) temperature in order to probe the evolution of the Mn local atomic structure across the magnetic transition. Finally we collected XAS spectra at the Mn *K*-edge for a pure $LaMnO_3$ (between 77 K and RT) and $CaMnO_3$ (at RT) samples and for two Mn oxides (at RT): Mn_3O_4 and Mn_2O_3, to be used as references.

The XAS spectra are usually divided into two main regions: the near-edge region, named XANES (x-ray absorption near-edge structure), extending up to some tens of eV above the edge, and the extended region, named EXAFS (extended x-ray absorption fine structure) starting some tens of eV above the edge. This discrimination has been introduced in order to roughly distinguish the information available in the two regions: the XANES features are mainly affected by the electronic nature of the absorber and by the topology of the atomic environment around it. The features in the EXAFS region are dominated by the structure of the first few neighboring shells around the absorber. A complete and reliable theory able to quantitatively describe the XANES region is still lacking. However, relevant qualitative or semiquantitative information on the nature and environment of the absorber can be derived comparing the data to that of reference compounds. The analysis of the EXAFS region, on the contrary, is more reliable and it represents a widely used tool to achieve an accurate description of the local atomic environment around the absorbing atomic species.[34] In the following sections we describe the results obtained from the analysis of Mn *K*-edge XAS data of our samples.

1. XANES region

The Mn *K*-edge XAS data were treated using the standard approach in order to extract the XANES normalized signals. First the experimental absorption spectra, $\alpha(E)=\ln(I_o/I_1)$, were corrected by subtracting the background absorption signal. The background has been simulated using the "Victoreen" empirical formula: $CE^{-3}-DE^{-4}$ whose coefficients (C,D) were determined by fitting the experimental XAS data in the energy region below the edge (6.3–6.52 keV). The corrected spectra were normalized to the free ion absorption so that the smooth part of the absorption coefficient above the edge, modeled with a polynomial function, is

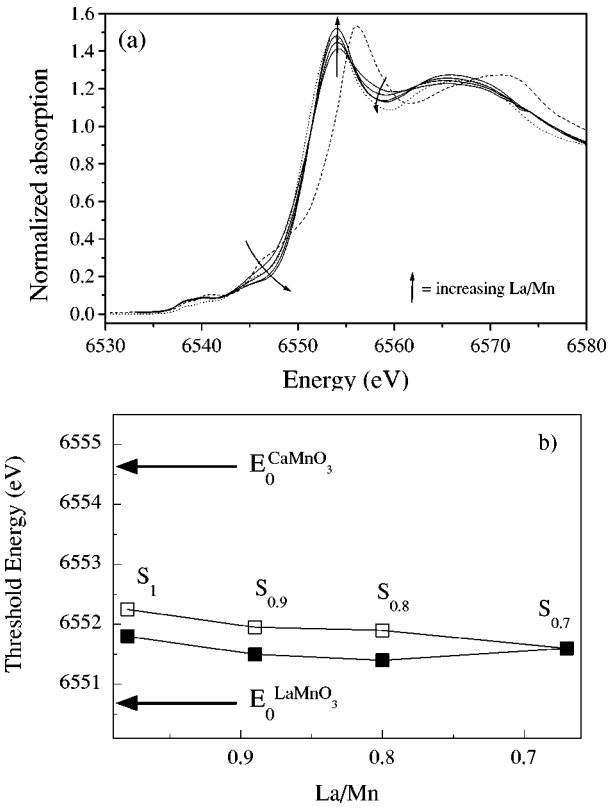

FIG. 5. (a) Normalized XANES spectra of samples S_1, $S_{0.9}$, $S_{0.8}$, and $S_{0.7}$ (full lines), compared to the XANES spectra of reference compounds $LaMnO_3$ (dot line) and $CaMnO_3$ (dash line); (b) threshold energies for S_i samples taken at the main inflection point (maximum of the first derivative) of the absorption spectrum (full squares) compared to the threshold energies calculated from sample titration (open squares).

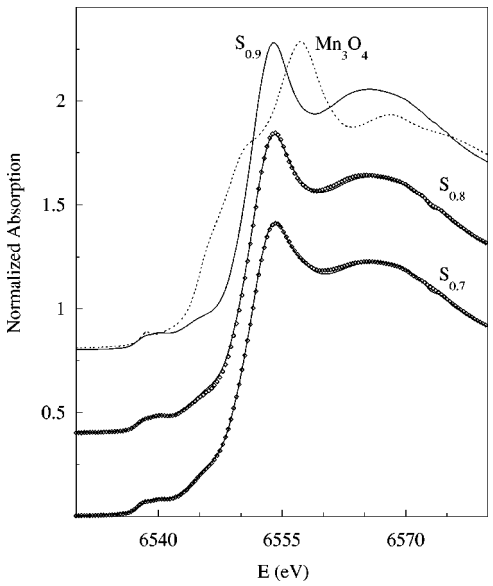

FIG. 6. Simulation (full lines) of XANES spectra (diamonds) of samples $S_{0.7}$ and $S_{0.8}$ from a linear combination of $S_{0.9}$ (full line, upper curves) and Mn_3O_4 (dot line, upper curves) XANES spectra (see text).

equal to 1. Figure 5(a) reports normalized XANES spectra for the S_i samples compared with those of reference compounds $LaMnO_3$ and $CaMnO_3$.

The threshold energies (E_0) were chosen at the main inflection point (maximum of the first derivative) of the absorption spectra. We found $E_0^{LaMnO_3}=6550.7(1)$ eV and $E_0^{CaMnO_3}=6554.6(1)$ eV, in good agreement with the values 6550.6 and 6654.8 eV reported in the literature.[35] In hole doped compounds, such as $La_{1-x}Ca_xMnO_3$, E_0 progressively shifts as a function of Mn^{4+} content.[35–37] In the S_i samples [Fig. 5(b)] we observe a weak (almost negligible) E_0 change (less than 0.4 eV) as the nominal Mn^{4+} doping varies between 22% ($S_{0.7}$) and 39% ($S_{0.9}$). This finding, in our samples, is likely to be related to the phase separation into $La_{\sim 0.9}MnO_3$ and Mn_3O_4 phases as suggested by XRD data analysis. In order to prove this hypothesis, we fitted the XANES of $S_{0.8}$ and $S_{0.7}$ samples (μ_{exp}) with a linear combination of XANES spectra of Mn_3O_4 and $La_{0.9}MnO_3$ (sample $S_{0.9}$):

$$\mu_{exp}=(1-\beta)\mu_{(La_{0.9}MnO_3)}+\frac{\beta}{3}\mu_{(Mn_3O_4)}.$$

The $S_{0.9}$ sample has been chosen because its nominal La/Mn ratio reaches the minimum value compatible with the phase diagram for La_2O_3-Mn_2O_3 solid solutions.[17] Such a linear combination fits well the experimental data (Fig. 6) and the relative amount of Mn_3O_4 and $La_{0.9}MnO_3$ phases matches well with the values derived from the XRD patterns refinement (Table III). The (weak) differences can also be an effect of the different sensitivity of the two techniques: XRD probing only the well crystallized phases, XAS probing the global Mn environment crystalline or amorphous. An attempt to fit the experimental XANES spectra of the $S_{0.8}$ and $S_{0.7}$ samples using the signal of the Mn_2O_3 reference sample

TABLE III. Composition of the samples as derived by analysis of XRD and XANES data. The relative uncertainty on Mn_3O_4 fractions are 3–5 % (XRD) and 5–10 % (EXAFS).

Sample	XRD	XANES
S_1	$0.97(La_{0.896}Mn_{0.978}O_3)+0.03(La_2O_3)$	
$S_{0.9}$	$La_{0.91}MnO_3$	$La_{0.9}MnO_3$
$S_{0.8}$	$0.9(La_{0.892}MnO_3)+0.03(Mn_3O_4)$	$0.87(La_{0.9}MnO_3)+0.04(Mn_3O_4)$
$S_{0.7}$	$0.76(La_{0.888}MnO_3)+0.08(Mn_3O_4)$	$0.8(La_{0.9}MnO_3)+0.07(Mn_3O_4)$

drastically reduces the quality of the fit and, in addition, the resulting sample composition does not match with ICP and XRD results.

2. EXAFS region

We exploited the analysis of the EXAFS spectra as a function of temperature to follow the evolution of the Mn local environment across the magnetic transition, to be compared with the peculiar behavior reported in substituted compounds. It is well known, in fact, that the magnetic transition in substituted compounds[35,38,39] is accompanied with a sudden reduction of structural distortions reflecting the weakening of electron to lattice coupling in the low-temperature ferromagnetic metallic phase.

The EXAFS structural signal $\chi(k)$ is defined as the relative oscillations of the total absorption coefficient $\mu(k)$ with respect to the absorption coefficient of the isolated atom $\mu_{\bigcirc}(k)$.[34]

$$\chi(k)=\frac{\mu(k)-\mu_{\circ}(k)}{\mu_{\circ}(k)}, \tag{1}$$

where $k=\hbar^{-1}[2m(E-E_o)]^{1/2}$ (Å^{-1}) is the photoelectron wave vector defined as a function of the x-ray photon energy E with respect to the energy of the absorption edge and m is the electron mass.

In single scattering approximation the theoretical EXAFS signal is given by the well-known formula[34]

$$k\chi(k)=S_o^2\sum_i \frac{N_i A_{oi}}{R_i^2}\sin(2kR_i+\phi_{oi})e^{-2\sigma_i^2k^2}e^{-2R_i/\lambda} \tag{2}$$

in which the sum runs over the neighbor coordination shells. For each shell N_i represents the coordination number, R_i the average distance, and σ_i^2 is the mean-square relative displacement (MSRD) of the absorber-scatterer pair. The $A_{oi}(k,R_i)$ and $\phi_{oi}(k,R_i)$ are respectively the backscattering amplitude and phase functions; $\lambda(k)$ is the photoelectron mean free path, and S_o^2 is an empirical parameter taking into account many-body losses in the photoabsorption process.

In the case of multiple-scattering (MS) processes an expression formally similar to Eq. (2) can apply in which R_i represents the full length of the MS path. However, the amplitude and phase functions become now complex expressions taking into account each scattering event along the multiple-scattering path. Moreover, the σ^2 factor becomes a complicated expression accounting not only for the variance of the MS path length but also including the effect of scattering angle distributions. MS contributions are usually weak, except for (almost-) collinear atomic arrangements in which they are enhanced by the large forward scattering amplitude[40] (focusing effect). In our samples significant MS signals have been found for the three body configurations Mn-O_1-Mn_1 ($\theta_{MnOMn}\sim 160°$) and Mn-La-Mn_3 ($\theta_{MnLaMn}\sim 180°$) in Fig. 7.

The EXAFS data analysis was performed following the theory described in Refs. 41 and 40 and implemented in the freely available GNXAS package.[42,43] This approach allows

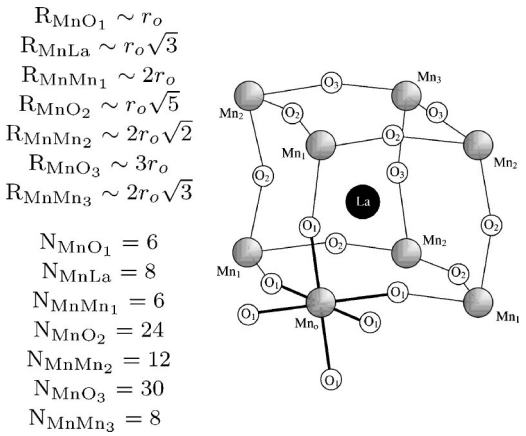

FIG. 7. Schematic representation of the perovskite pseudocubic unit. The generic Mn absorber is surrounded by a Jahn-Teller distorted octahedron of six oxygen atoms (O_1). The La ions are at the center of the pseudocube and the other Mn and O neighbors are labeled as a function of their distance from the absorber. Approximate distance and coordination number for each shell are reported on the left.

taking into account single- as well multiple-scattering contributions to the EXAFS structural signal. The absorption background has been simulated with a straight line fitting the experimental data in the pre-edge region. The atomic absorption in the post-edge region has been simulated with a smoothly varying polynomial spline through the experimental data. In order to choose the relevant contributions to be used in the fitting we proceeded as follows: after a best fit is achieved for the nearest-neighbor shell (MnO_6 octahedron), a new contribution is added, chosen on the basis of the crystallographic structure and of its relative multiplicity (Fig. 7), and a new refinement is performed. An F test is then made and the new contribution is retained only if it improves the statistical significance of the fitting. In such a way we were able to fit the XAS signal reproducing the main structural features until about 7 Å around the absorber as depicted in Figs. 9 and 10.

In order to obtain physically reliable best-fit results the number of free parameters and the correlations within them must be kept as low as possible through a suitable choice of constraints and approximations. To this aim the multiplicity of each contribution was fixed to the value expected from the crystallographic structure. The same $S_o^2=0.85$, experimentally determined refining the $LaMnO_3$ EXAFS data, was kept for all the samples. Finally we neglected the contributions of parasitic Mn_3O_4 phases.

In order to motivate this last choice we first notice that the Mn_3O_4 phase is poorly crystallized (see XRD results), thus the EXAFS signal is likely to be strongly attenuated by the exponential Debye-Waller (DW) term $e^{-2\sigma^2k^2}$ in Eq. (2). Notice that the effect of disorder decreases in the XANES region (i.e., for $k\sim 0$); this justifies the larger sensitivity of XANES to the parasitic Mn_3O_4 phase. In addition, the Mn_3O_4 structure has two inequivalent Mn sites[44] one having four oxygen ions at about 2.08 Å, the other being sixfold coordinated with four O around 1.90 Å and two O around

TABLE IV. The main parameters characterizing the local structure around Mn ions as derived by EXAFS analysis: the average values (upper numbers) with minimum and maximum values (middle numbers) are reported. The average error bars on the refined parameters are also reported (lower numbers). In all the S_i samples/temperatures the Mn-Mn_1 distances are 3.81(4) Å while the Mn-Mn_1 Debye-Waller factors increase from ~0.006(1) to ~0.011(2) Å^2 going from S_1 to $S_{0.7}$. In $LaMnO_3$ R(Mn-Mn_1) is found 3.89(5) Å while σ^2 is ~0.02(4) Å^2. The effect of cooling is smaller than the error bars.

	MnO_1		MnLa		$MnMn_2$		MnO_3		Mn-O_1-Mn_1
	R (Å)	σ^2 ($\times 10^3$ Å^2)	R (Å)	σ^2 ($\times 10^3$ Å^2)	R (Å)	σ^2 ($\times 10^3$ Å^2)	R (Å)	σ^2 ($\times 10^3$ Å^2)	θ (°)
$LaMnO_3$	1.92	1.7	3.36	14.3	5.57	8.7	5.84	18.9	158.6
	1.91–1.92	1.2–2.3	3.35–3.37	13–15	5.51–5.57	7–11	5.79–5.89	16–23	157.6–159.5
	(±.01)	(±.2)	(±.02)	(±1)	(±.04)	(±1)	(±.04)	(±2)	(±1)
	2.13								
	2.11–2.14								
	(±.01)								
S_1	1.93	5.6	3.36	8.3	5.56	7.6	5.75	9.1	163.4
	1.91–1.92	4.2–6.9	3.35–3.36	7.8–9.2	5.53–5.54	6.6–8.6	5.74–5.75	7.4–9.9	161–165
	(±.01)	(±.5)	(±.02)	(±1)	(±.04)	(±1)	(±.03)	(±1)	(±1)
$S_{0.9}$	1.93	7.7	3.36	8.7	5.55	8.5	5.77	9.2	162.5
	1.93–1.93	6–9.5	3.35–3.36	6.4–10.5	5.54–5.55	7–9.8	5.74–5.78	8.3–10.4	160.8–164.7
	(±.01)	(±.7)	(±.02)	(±1)	(±.04)	(±1)	(±.04)	(±1)	(±1)
$S_{0.7}$	1.93	8.6	3.36	11.0	5.54	10.2	5.75	11.9	163.7
	1.93–1.94	6.3–11.5	3.36–3.38	9.2–13.4	5.53–5.56	8.3–13.8	5.74–5.78	9.7–14	160.3–163.7
	(±.01)	(±.8)	(±.03)	(±1)	(±.04)	(±1)	(±.05)	(±1)	(±1)

2.29 Å. The complex Mn-O distribution in Mn_3O_4 and the broad distribution expected in the perovskite phase (either due to the MnO_6 JT distortions, or to the nanocrystalline nature of our UASP samples) makes it difficult to distinguish the two contributions.

Owing to these limitations EXAFS is less sensitive than XANES to the parasitic phases. Neglecting these phases would bias the absolute structural results. Nevertheless, it would not affect the relative structural changes observed (see below) tuning the sample temperature across the magnetic transition.

The relevant structural parameters derived from the fitting are reported in Table IV and best-fit examples are reported in Figs. 9 and 10. The main structural features can be grouped in four main regions corresponding to the four main peaks in the FT's (Figs. 8 and 9). The first region, corresponding to the main peak in the FT around 1.5 Å, concerns the nearest-neighbor signal (notice that the FT's are uncorrected for the phase-shift effect). Two signals were required in order to fit the contribution of Jahn-Teller distorted MnO_6 octahedra in $LaMnO_3$ (Fig. 9, left panel): four oxygen atoms were found at about 1.92 Å ($\gamma^{(2)}_{MnO_{1a}}$), and two around 2.13 Å ($\gamma^{(2)}_{MnO_{2b}}$).

We are not able to distinguish the subshell splitting of the first MnO_{1a} shell, expected around 1.9 and 1.97 Å.[29] The longer Mn-O distance appears shorter than in the crystallographic structure (i.e., 2.17 Å). This could be an effect of the correlated disorder on Mn and O sites and/or due to the weaker sensitivity of EXAFS to longer distances. The Debye-Waller factor σ^2_{MnO} was kept the same for the two contributions MnO_{1a} and MnO_{1b} in order to reduce correlation effects.[39] This choice is partially not justified due to the bimodal nature of the MnO_{1a} contribution. Nevertheless, the relevant parameter to be compared with the doped samples is the variance of the Mn-O distribution being defined as

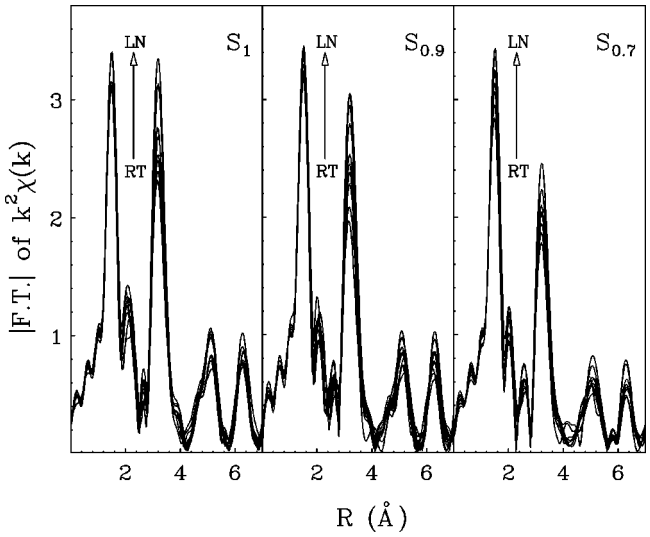

FIG. 8. Modulus of the fourier transform (FT) of the EXAFS data for the three samples investigated. The peaks signal the occurrence of an atomic correlation but the peak positions do not reflect the real interatomic distance owing to the phase shift effect.[34] The FT peak intensities increases as the temperature decreases indicating the ordering of the local atomic structure around Mn ions.

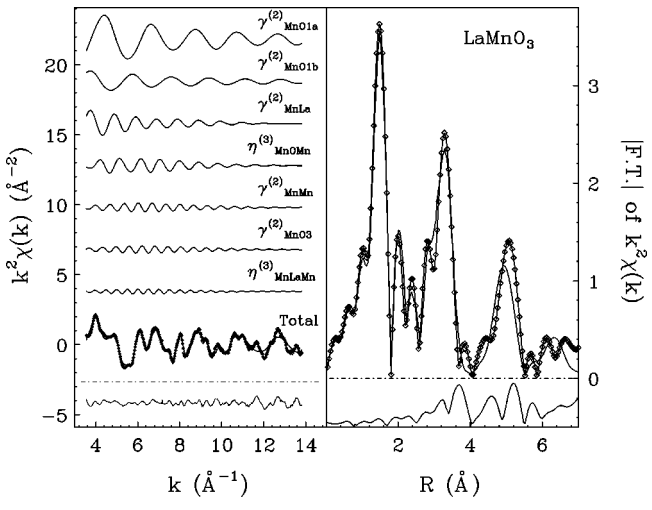

FIG. 9. Example of best fit on the $LaMnO_3$ sample: the left panel reports the partial signals used (vertically shifted for clarity). The total EXAFS signal (dots) and the total theoretical signals (full line) are shown together with the residual (experimental minus theoretical data) (lower curve). The right panel reports the modulus of the Fourier transform (FT) of the experimental (dots) and theoretical (line) signals and the FT of the residual (lower shifted for clarity).

$$\sigma^2_{Tot}=\frac{2(R_{1a}-\langle R\rangle)^2+(R_{1b}-\langle R\rangle)^2}{3}+\sigma^2_1,$$

where $\langle R\rangle$ is the average Mn-O bond length. The $\sigma^2_{Tot}(T)$, reported in Fig. 11, is in good agreement with literature data.[38,45]

A single contribution is required to fit the MnO_6 distribution in self-doped samples (Fig. 10). The difficulty in distinguishing a subshell distribution in doped samples is well known in hole doped compounds[35,38,39] as a result of reduced JT effect with respect to the undoped compounds. In addition, the nanocrystalline nature of our samples and the presence of parasitic phases contribute to enlarge the MnO distribution making it hard to reveal an eventual subshell distribution. Interestingly the σ^2_{MnO} (around RT) increases from $\sim 6\times10^{-3}$ Å^2 in S_1 to $\sim 11\times10^{-3}$ Å^2 in $S_{0.7}$. This increment could be related to the increasing Mn_3O_4 contamination.

The σ^2_{MnO} in doped samples decreases steeply cooling the sample across the MI transition. This trend, not observed in pure $LaMnO_3$, is well known in substitutional doped manganese perovskites and reflects the reduction of structural distortions through the insulator to metal transition due to the weaker charge to lattice coupling. This finding demonstrates that in our samples the magnetic transition has a similar origin.

In the second region we found the two-body contributions of 8 MnLa and 12 Mn-O_1-Mn_1 configurations (Fig. 7). Notice that the structural parameters for three-body Mn-O_1-Mn_1 and two-body Mn-Mn_1 distributions are no longer independent; then their sum is treated by GNXAS as a single contribution named η^3_{MnOMn} in Figs. 9 and 10 (see Ref. 42 for more details). The Mn-La coordination distance is around 3.36 Å in $LaMnO_3$ as well as in vacancy doped compounds and does not change as a function of temperature. The σ^2_{MnLa} is larger for $LaMnO_3$ than in doped compounds. This finding comes in agreement with the broader Mn-La distribution in the pure $LaMnO_3$ structure (orthorhombic structure)[29] with respect to that found in doped compounds (rhombohedral structure). The σ^2_{MnLa} decreases smoothly as a function of temperature in all the samples evidencing a weak participation of Mn-La shell to the magnetic transition in agreement with the literature.[36]

The average Mn-O_1-Mn_1 bond angle in pure $LaMnO_3$ is $\theta_{MnOMn}\sim 159°$ and does not change appreciably on cooling the sample until 77 K. In doped compounds the average $\theta_{MnOMn}\sim 163°$ is in agreement with XRD results (Table II). However, θ_{MnOMn} increases significantly upon cooling the samples across T_C (Fig 11). This behavior is consistent with

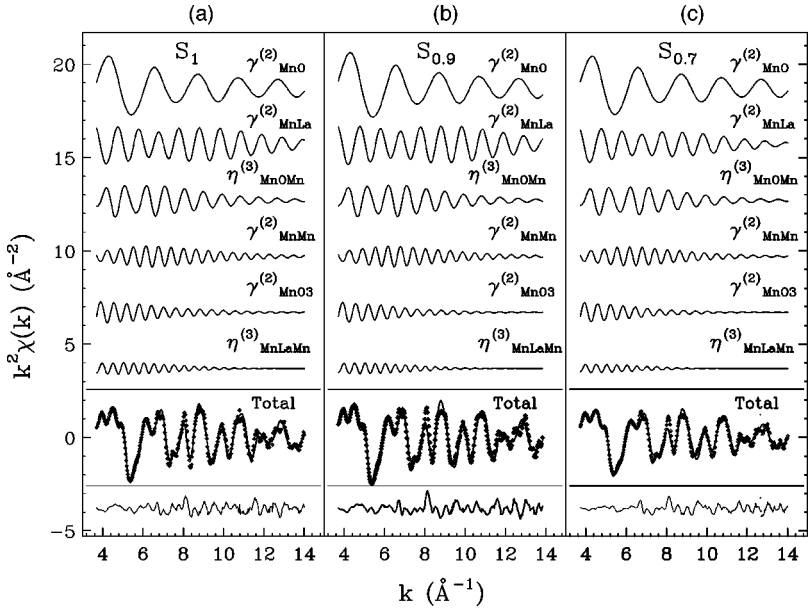

FIG. 10. Examples of best fit on vacancy doped samples at the LN temperature: S_1 [panel (a)], $S_{0.9}$ [panel (b)], and $S_{0.7}$ [panel (c)]. The upper curves represent the signals used, below are shown experimental (dots) and total theoretical (full line) signals. The residuals are reported below.

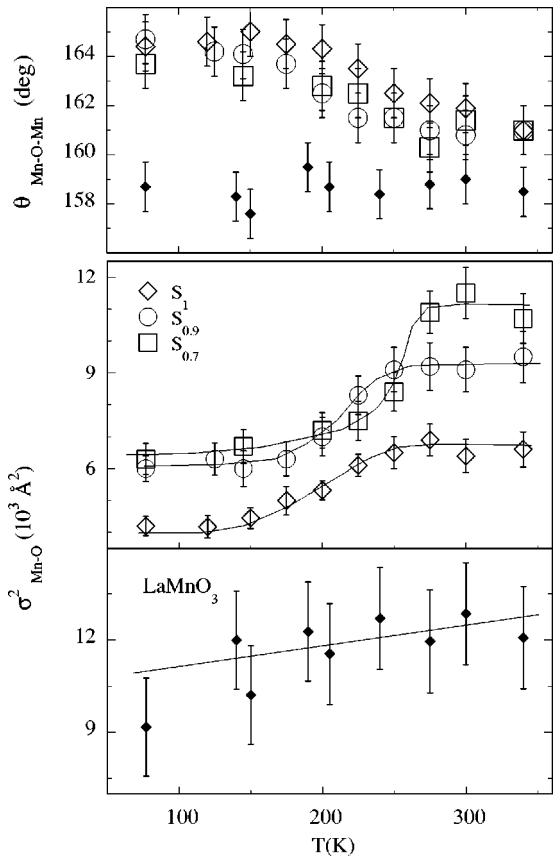

FIG. 11. Lower panel: variance of Mn-O bond length distribution in $LaMnO_3$ as a function of temperature (see text). Middle panel: Debye-Waller factors of Mn-O bond length distribution as a function of temperature in vacancy-doped samples. Upper panel: Mn-O-Mn bond angle distribution in $LaMnO_3$ and in vacancy-doped samples.

the increase of θ_{MnOMn} observed by neutron diffraction[30] on $La_{0.75}Ca_{0.25}MnO_3$, when the sample is cooled across T_C.

The third structural region includes the contributions of Mn-Mn_2 and Mn-O_3 pairs (Fig. 7) while the contributions of Mn-O_2 are negligibly weak due to a huge Debye-Waller term ($\sigma^2_{MnO_2} > 0.04$ Å^2). Coordination distances for Mn-Mn_2 and Mn-O_3 pairs are in agreement with the crystallographic structure (Table IV) and do not change significantly as a function of temperature. The larger $\sigma^2_{MnO_3}$ in $LaMnO_3$ is consistent with higher structural distortions in undoped compounds.[29,30] Both $\sigma^2_{MnMn_2}$ and $\sigma^2_{MnO_3}$ increase as a function of composition from S_1 to $S_{0.7}$; this trend should be related to the increasing fraction of the Mn_3O_4 phase in the $S_{0.7}$ sample.

In the fourth region, around 6 Å (Fig. 8), we found the signal of Mn-La-Mn_3 atomic configurations, enhanced by the large focusing effect. The sum of Mn-La-Mn_3 and Mn-Mn_3 contributions is included as $\eta^{(3)}_{MnLaMn}$ in Figs. 9 and 10. The only free parameter was the Mn-La-Mn angle that remains around 180° without any special trend with temperature.

EXAFS results demonstrate that cooling the sample mainly affects the evolution of MnO_6 distortions and Mn-O-Mn bond angles. In particular, the evolution of σ^2_{MnO} and θ_{MnOMn} in the doped samples shows a broad discontinuity near T_C, in contrast with the smooth trend found in the $LaMnO_3$ sample. This trend, accordingly with results on substituted manganites,[46] demonstrates that also in vacancy doped compounds the insulator to metal transition has structural counterparts, corresponding to the decrease of MnO_6 JT distortions and the opening of the Mn-O-Mn bond angle.

III. DISCUSSION AND CONCLUSION

Ultrasonic assisted spray pyrolysis allows producing rapidly a large amount of vacancy doped Mn-oxide perovskites in the form of nanocrystalline powders. This technique provides accurate reproducibility of sample microstructure and magnetic properties, highly suitable for applicative purpose. Recent studies highlighted some peculiar aspects in the evolution of the magnetic properties of these compounds. In particular, it has been observed that the Curie temperature and the sharpness of the magnetic transition increase as the nominal composition ratio decreases until La/Mn$\sim$0.9, then they remain almost unchanged for La/Mn$\leqslant$0.9. Moreover, the saturation magnetization reaches a maximum value at an average composition of La/Mn$\sim$0.9.

In order to achieve an accurate sample characterization several complementary techniques have been exploited. The sample composition and Mn^{4+} content were determined by ICP and titration, respectively. Powder particle morphology was described by SEM and TEM investigations. Rietveld profile refinement of XRD patterns allowed us to probe the structure and composition of crystallized phases. The comparative analysis of the XANES region of XAS spectra has definitively assessed and quantified the amount of the Mn_3O_4 parasitic phase. Finally, the analysis of the EXAFS spectra as a function of temperature allowed us to describe the evolution of the Mn local structure in vacancy doped perovskite phase across the magnetic transition.

Our findings demonstrate that for La/Mn$<$0.9, the structure is no longer stable and separates into a vacancy doped La$\sim$0.9MnO_3 phase and in a Mn_3O_4 phase. The La/Mn ratio in the vacancy doped perovskite phase is largely unaffected by changes in the average composition. This fact explains the similar magnetic transition observed for samples $S_{0.9}$, $S_{0.8}$, and $S_{0.7}$. Recent studies on well-crystallized samples[18] directly observed the parasitic Mn_3O_4 phase giving strength to our finding. In our case, dealing with nanocrystalline samples, the proposed methodology cannot be directly applied since Mn_3O_4 may evade XRD detection due to its small crystallite size. Nevertheless, the XANES analysis gave direct proof of the phase separation and, in addition, reliably quantified the relative amount of each phase.

Temperature-dependent EXAFS measurements demonstrated the reduction of MnO_6 distortions and the lining up of Mn-O-Mn bond angles when the samples were cooled into the FM metallic phase. This trend is very similar to the one observed in substituted compounds such as $La_{1-x}Ca_xMnO_3$.[45–47] It then appears that the same mechanism is responsible for the magnetic transition in both classes of samples. This mechanism, involving the weakening of the charge to lattice interaction and the strengthening of the DE

coupling, has a structural counterpart corresponding to the reduction of the JT effect on Mn sites.

The observed differences in magnetic properties between La/Mn$\leqslant$0.9 samples and S_1 could not be only attributed to variations of structural properties since XRD and XAS analysis, respectively, sensitive to the crystallographic properties and to the local order features such as Mn-O distances and Mn-O-Mn bond angles, demonstrated only minor differences in the structure. Thus, for sample S_1, the broadening of the transition and the reduced Curie temperature are probably related to vacancies on the manganese site. Such kind of defects may hinder the charge mobility reducing the DE interaction and favoring the superexchange, leading to a distribution of sign and strength of magnetic interactions, and in a lowering of T_C.

ACKNOWLEDGMENTS

The authors acknowledge the excellent technical support of F. Campolungo, V. Sciarra, and V. Tullio (INFN-LNF) in optimizing the GILDA beamline setup. Dr. S. Pascarelli and A. Sophia are kindly acknowledged for manuscript revision. The GILDA beamline is financed by the Italian institutions CNR, INFM, and INFN.

*Corresponding author. Electronic address: meneghini@fis.uniroma3.it

[1] R. von Helmolt, J. Wecker, B. Holzapfel, L. Schultz, and K. Samwer, Phys. Rev. Lett. **71**, 2331 (1993).
[2] B. Salamon and M. Jaime, Rev. Mod. Phys. **73**, 583 (2001).
[3] C. Zener, Phys. Rev. **82**, 403 (1951).
[4] P. Anderson and H. Hasegawa, Phys. Rev. **100**, 675 (1955).
[5] P. de Gennes, Phys. Rev. **118**, 141 (1960).
[6] J. Töpfer and J.B. Goodenough, Chem. Mater. **9**, 1467 (1997).
[7] R. Mahendiran, S.K. Tiwary, A.K. Raychaudhuri, T.V. Ramakrishnan, R. Mahesh, N. Rangavittal, and C.N.R. Rao, Phys. Rev. B **53**, 3348 (1996).
[8] J.B. Goodenough, Solid State Ionics **94**, 17 (1997).
[9] H. Jena, K.V.G. Kutty, and T.R.N. Kutty, J. Alloys Compd. **350**, 102 (2003).
[10] J.A. Alonso, M.T. Casais, M.J. Martinez-Lope, and I. Rasines, J. Solid State Chem. **129**, 105 (1997).
[11] I. Maurin, P. Barboux, Y. Lassailly, J.-P. Boilot, and F.J. Villain, J. Magn. Magn. Mater. **211**, 139 (2000).
[12] A. Arulraj, R. Mahesh, G.N. Subbanna, R. Mahendiran, A.K. Raychaudhuri, and C.N.R. Rao, J. Solid State Chem. **127**, 87 (1996).
[13] V. Ferris, L. Brohan, M. Ganne, and M. Tournoux, Eur. J. Solid State Inorg. Chem. **32**, 131 (1995).
[14] B.C. Hauback, H. Fjellvaeg, and N. Sakai, J. Solid State Chem. **124**, 43 (1996).
[15] M. Hervieu, R. Mahesh, N. Rangavittal, and C.N.R. Rao, Eur. J. Solid State Inorg. Chem. **32**, 79 (1995).
[16] S. deBrion, F. Ciorcas, G. Chouteau, P. Lejay, P. Radaelli, and C. Chaillout, Phys. Rev. B **59**, 1304 (1999).
[17] J.V. Roosmalen, H. Zanbergen, E.H.P. Cordfunke, W.L. Ijdo, and D.J.W. Ijdo, J. Solid State Chem. **114**, 516 (1995).
[18] J.A. Joy, C.R. Sankar, and S.K. Date, J. Phys.: Condens. Matter **14**, L663 (2002).
[19] P. Murugavel, M. Kalaiselvam, A. Raju, and C.N.R. Rao, J. Mater. Chem. **7**, 1433 (1997).
[20] W. Pyda, J. Eur. Ceram. Soc. **17**, 121 (1997).
[21] E. Djurado and E. Meunier, J. Solid State Chem. **141**, 191 (1998).
[22] G. Dezanneau, Ph.D. thesis, Institut National Polytechnique de Grenoble (INPG), Grenoble, France, 2001.
[23] I.G. Andersen, E. Andersen, P. Norby, and E. Skou, J. Solid State Chem. **113**, 320 (1994).
[24] H. Y. Hwang and S.-W. Cheong, *Ferromagnetism vs. Charge/Orbital Ordering in Mixed-Valent Manganites* (Gordon & Breach, London, 1999), Chap. 9.
[25] L. Balcells, B. Martinez, F. Sandiumenge, and J. Fontcuberta, J. Magn. Magn. Mater. **211**, 193 (2000).
[26] G. Dezanneau, A. Sin, H. Roussel, H. Vincent, and M. Audier, J. Solid State Chem. **121**, 133 (2002).
[27] H.M. Rietveld, Acta Crystallogr. **22**, 151 (1967).
[28] J. Rodriguez-Carvajal, ''FULLPROOF: A program for Rietveld Refinement and Pattern Matching Analysis,'' in *Abstracts of the Satellite Meeting on Powder Diffraction of the XV Congress of the IUCR*, Toulouse, France (1990), p. 127.
[29] Q. Huang, A. Santoro, J.W. Lynn, R.W. Erwin, J.A. Borchers, J.L. Peng, and R.L. Greene, Phys. Rev. B **55**, 14 987 (1997).
[30] P.G. Radaelli, G. Iannone, M. Marezio, H.Y. Hwang, S.W. Cheong, J.D. Jorgensen, and D.N. Argyriou, Phys. Rev. B **56**, 8265 (1997).
[31] B.C. Tofield and W.R. Scott, J. Solid State Chem. **10**, 183 (1974).
[32] J.F. Mitchell, D.N. Argyriou, C.D. Potter, D.G. Hinks, J.D. Jorgensen, and S.D. Bader, Phys. Rev. B **54**, 6172 (1996).
[33] S. Pascarelli, F. Boscherini, F. D'Acapito, J. Hrdy, C. Meneghini, and S. Mobilio, J. Synchrotron Radiat. **3**, 147 (1996).
[34] P.A. Lee, P.H. Citrin, P. Eisenberger, and B.M. Kinkaid, Rev. Mod. Phys. **53**, 769 (1981).
[35] G. Subías, J. García, M.G. Proietti, and J. Blasco, Phys. Rev. B **56**, 8183 (1997).
[36] F. Bridges, C.H. Booth, M. Anderson, G.H. Kwei, J.J. Neumeier, J. Snyder, J. Mitchell, J.S. Gardner, and E. Brosha, Phys. Rev. B **63**, 214405 (2001).
[37] Q. Qian, T.A. Tyson, C.-C. Kao, M. Croft, S.-W. Cheong, G. Popov, and M. Greenblatt, Phys. Rev. B **64**, 024430 (2001).
[38] C.H. Booth, F. Bridges, G.H. Kwei, J.M. Lawrence, A.L. Cornelius, and J.J. Neumeier, Phys. Rev. B **57**, 10 440 (1998).
[39] C. Meneghini, C. Castellano, S. Mobilio, A. Kumar, S. Ray, and D.D. Sarma, J. Phys.: Condens. Matter **14**, 1967 (2002).
[40] A. Filipponi, A. DiCicco, and C.R. Natoli, Phys. Rev. B **52**, 15 122 (1995).
[41] M. Benfatto, C.R. Natoli, A. Bianconi, J. Garcia, A. Marcelli, M. Fanfoni, and I. Davoli, Phys. Rev. B **34**, 5774 (1986).
[42] A. Filipponi and A. DiCicco, Phys. Rev. B **52**, 15 135 (1995).
[43] A. Filipponi and A. DiCicco, TASK Q. **4**, 575 (2000).
[44] K. Satomi, J. Phys. Soc. Jpn. **16**, 258 (1961).
[45] C. Meneghini, R. Cimino, S. Pascarelli, S. Mobilio, C. Raghu, and D.D. Sarma, Phys. Rev. B **56**, 3520 (1997).
[46] G. Subías, J. García, J. Blasco, and M.C.S.M.G. Proietti, J. Phys.: Condens. Matter **14**, 5017 (2002).
[47] C.H. Booth, F. Bridges, G.J. Snyder, and T.H. Geballe, Phys. Rev. B **54**, 15 606 (1998).